Thermal Analysis and Simulation of the Superconducting Magnet in the SpinQuest Experiment at Fermilab

Z. Akbar*and D. Keller†

University of Virginia

November 18, 2020

Abstract

The SpinQuest experiment at Fermilab aims to measure the Sivers asymmetry for the $\bar{u}$ and $\bar{d}$ sea quarks in the range of $0.1 < x_B < 0.5$ using the Drell-Yan production of dimuon pairs. A nonzero Sivers asymmetry would provide an evidence for a nonzero orbital angular momentum of sea quarks. The proposed beam intensity is 1.5×10^{12} of 120 GeV unpolarized proton/sec. The experiment will utilize a target system consisting of a 5T superconducting magnet, NH_3 and ND_3 target material, a ^{4}He evaporation refrigerator, a 140 GHz microwave source and a large pumping system. The expected average of the target polarization is 80% for the proton and 32% for the deuteron. The polarization will be measured with three NMR coils per target cell.

A quench analysis and simulation of the superconducting magnet is performed to determine the maximum intensity of the proton beam before the magnet transitions to a resistive state. Simulating superconductor as they transition to a quench is notoriously very difficult. Here we approach the problem with the focus on producing an estimate of the maximum allowable proton beam intensity given the necessary instrumentation materials in the beam-line. The heat exchange from metal to helium goes through different transfer and boiling regimes as a function of temperature, heat flux, and transferred energy. All material properties are temperature dependent. A GEANT-4 based simulation is used to calculate the heat deposited in the magnet and the subsequent cooling processes are modeled using the COMSOL Multiphysics simulation package. This document serves as a technical note which explains the details of the quench analysis and simulations.

*Email: za2hd@virginia.edu

†Email: dustin@jlab.org

Contents

1 Introduction

The SpinQuest experiment will use a dynamically polarized target which has been constructed to meet the experimental specifications for the physics goals of measuring the Sivers function of the sea-quarks. The target system includes a 5T NbTi (Niobium-Titanium) superconducting split pair magnet as shown in figure 1. The coils are impregnated with epoxy and and held in place by the 316L stainless steel former. Superconductors only exhibit zero electrical

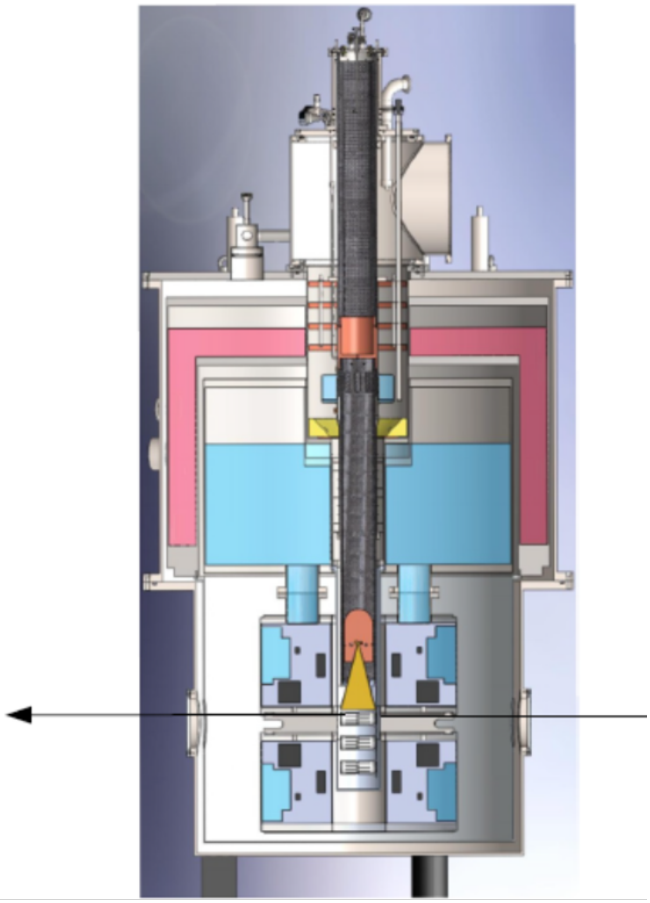

Figure 1: The cross-section of the magnet dewar. The black arrow shown in the cartoon is the proton-beam direction. The blue color represent the liquid helium and the pink color is the liquid nitrogen used for thermal shielding. Three target cups also shown in the picture along with the gold-copper horn to terminate the microwave.

resistance below a critical surface, dependent on temperature, current density and the strength of the magnetic field as shown in figure 2. Superconductivity

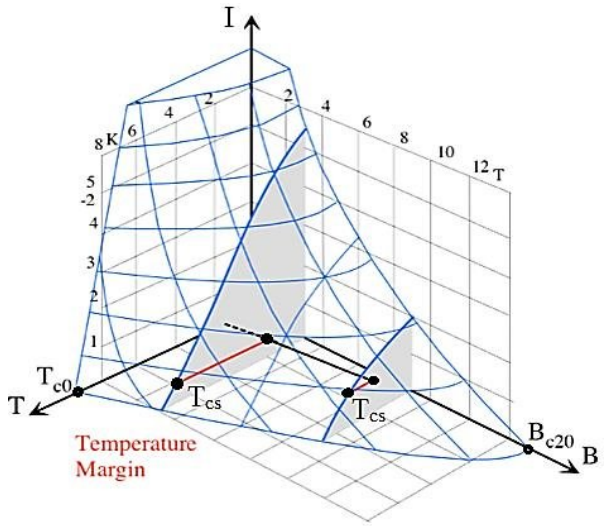

Figure 2: The critical surface of the NbTi superconductor.

prevails everywhere below this surface and resistivity everywhere above it. In the superconducting state, the resistivity of the NbTi filament is zero. NbTi is a type II superconductor which is capable of carrying high-current density at high-magnetic fields. The magnet coils are cooled with liquid helium using a pool boiling reservoir around the coils at a temperature of approximately 4.2 K.

When the temperature in the coils carrying high current density exceed the critical temperature T_c, the resistivity rapidly increase leading to joule heating that can melt the superconducting filaments in a short period of time. To prevent the superconductor from exceeding the critical temperature, the superconducting filaments are embedded in a copper matrix with low electrical resistivity. Figure 3 shows the NbTi type of superconducting wire where tiny (7 μm) Nb-Ti filaments are bundled together in a number of hexagons and embedded in a copper matrix.

Quenching is the process when some part of the superconductor transitions to resistive leading to loss of the magnetic field and the dumping of the energy stored in the coils into the liquid helium reservoir. This results in helium escaping from the cryogenic bath extremely rapidly usually leading to loss of helium and data taking time in the scattering experiment. During a quench in a particular wire, as the resistivity of the normal conducting filaments is an orders of magnitude higher than that of copper, the current deviates into the copper matrix and generates Joule heating. If the rate of heat generation is greater than the rate of heat transfer to the liquid helium, the quench will propagate through the entire magnet. Without quench protector this processes would damage the coils. The quench-protector circuit is a set of diodes and resistors that allows the coils to de-energize safely. The quench protector cir-

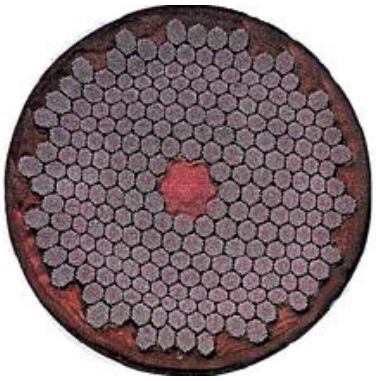

Figure 3: A typical of the NbTi strand.

cuit restricts the development of of potentially high voltage in the event of a quench. The protection circuit is fitted with barrier diodes and will not pass current until a certain voltage is exceeded. Under quench condition, the barrier voltage is exceeded and the protection circuit shunt a proportion of the current away from the magnet windings. The superconducting magnet consist of several coils, each with its own protection circuit. The equivalent circuit of a typical superconducting magnet is shown in figure 4 below

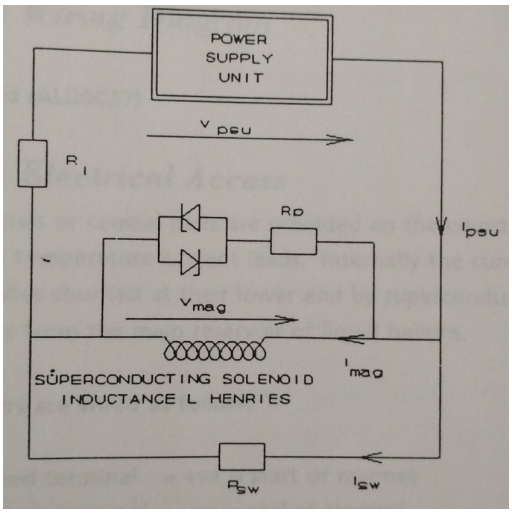

Figure 4: Equivalent circuit of a typical superconducting magnet. The barrier diodes shunt a proportion of the current away when a certain voltage is exceeded.

The superconducting magnet power supply (Oxford Instrument Mercury iPS) also provide additional quench protection. The Mercury iPS continually monitors the voltage produced across the magnet terminals. If the voltage

exceeds a programmed value for a programmed time, a quench is flagged. The Mercury iPS then ramps the magnet current down to zero at a controlled rate. The Mercury iPS also switches the current through high-power resistors inside the unit, which dissipate stored energy from the magnet.

Unexpected quenching can be very expensive and can considerable hinder the schedule of an experiment because most of the 140 L of liquid helium in the coil reservoir is vaporized. After a quench the magnet needs to be re-cooled and then re-energize to full field again. Together this takes about 3-4 hours. It is for these reasons that avoiding magnet quenching is critical to the success of SpinQuest and other solid polarized target experiments.

In order to protect the magnet, a quench needs to be avoided. For this, a proper understanding of how the magnet temperature increase due to the external heat source is essential. A 120 GeV proton beam of high intensity (up to 1.5×10^{12} protons/sec) will be delivered to the polarized target with the spill length of 4.4 s per minute.

The 120 GeV proton beam is provided by Fermilab Main Injector (FMI). A Radio Frequency Quadrupole (RFQ) accelerates the ions to about 750 KeV. In this section the proton beam acquires a 53.1 MHz Radio Frequency (RF) structure. The protons are accelerated to 8 GeV at LINAC and Booster before being injected to FMI. Protons are grouped into RF buckets which is 1-2 ns long. The time between each successive bucket is 1/53.1 MHz = 18.8 ns. A group of 84 RF bucket is called a "train". Typically, 82 out of 84 RF-buckets are filled with protons. Fermilab Main Injector can hold seven trains. Six trains out of seven trains are in use. Therefore, FMI holds 492 RF buckets which are filled with protons. Every minute protons are delivered to the target with the spill length of 4.4 s.

The beam intensity varies from empty RF buckets to very high intensity ones. Sometimes the beam intensity is so high that the track reconstruction pattern recognition algorithm simply fails to identify any tracks due to too many detector hits. Under such circumstances, the detector undergoes a "splat". The splat could also trigger magnet quench. This issue is discussed in section 6. Figure 5 shows the production of the proton beam and the micro structure of the beam.

The beam profile at SpinQuest is distinctly Gaussian with a Lorentzian tails. The spatial and temporal profiles of the beam are shown in figure 11 and 28. These tails can be problematic for the superconducting coils. An upstream beam collimator was installed for both matching the beam profile to the dimensions of the polarized target vertically and horizontally and reduction of beam tails colliding with the target magnet. The aperture of the collimator is 7.82 cm $\times$ 3.48 cm.

The heat generated in the superconducting magnet from the beam-target interactions over the duration of the beam spill (4.4 s) must be managed with the cooling from the pool boiling liquid helium reservoir that the coils sit in. If the rate of heat generation in the superconducting magnet persists to be greater than the rate of heat transfer to the liquid helium the temperature of the magnet increases and may exceed the critical surface. Therefore, a proper

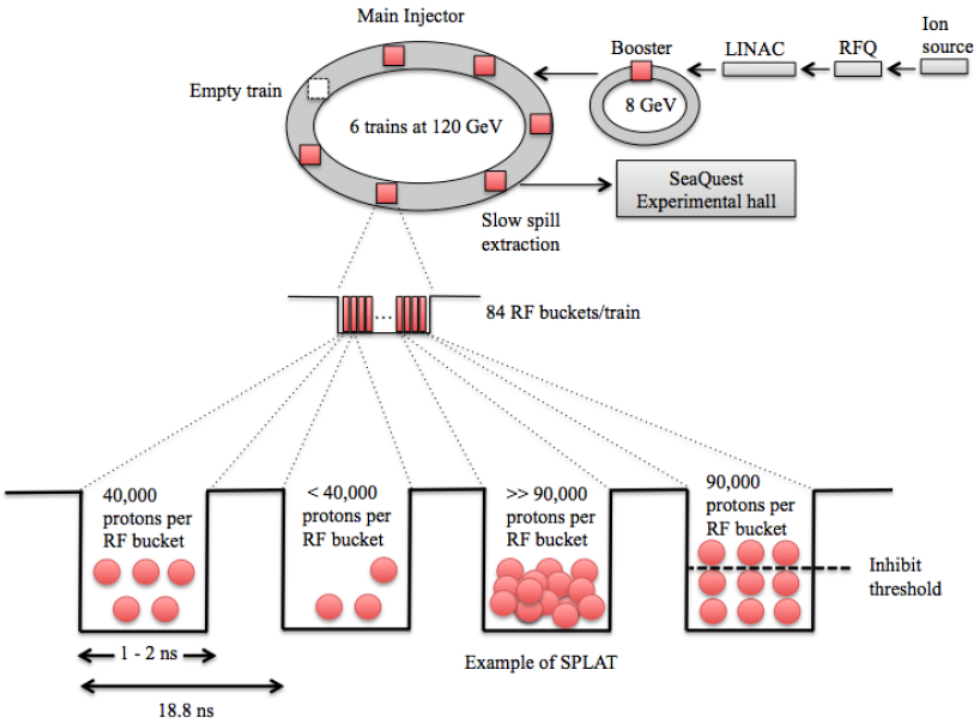

Figure 5: The production of the 120 GeV proton beam at Fermilab. Also shown the Micro structure of the beam along with examples of low intensity and high intensity buckets.

thermal analysis and simulation of the superconducting magnet is necessary to estimate the maximum proton intensity that can be delivered before a magnet quench.

The thermal analysis and simulations require many parameters which depend on the magnitude of the magnetic field inside the magnet. Therefore, the magnetic field inside the superconducting magnet needs to be determined precisely. Measurements of the external magnetic field where taken with a Hall Probe from Lakeshore Gaussmeter with an accuracy of 20 mT. Measurements were also taken from the inside of the nose with an NMR system. We have combined the measurement and simulation method to build a three-dimensional map of the magnetic field inside and around the superconducting magnet. Therefore, The magnetic-field mapping inside the magnet dewar and the thermal analysis and simulation of the NbTi superconducting magnet are the two main processes described in this analysis note.

The next section describes how the three-dimensional map of the field inside the magnet dewar was determined. using the field map is is possible to proceed

with the thermal analysis and simulation of the external heat sources, cooling processes by the liquid helium, and thermal properties of the materials. The simulation process using COMSOL is detailed in the following section. We then discuss the quench threshold, beam stability issue and the effect of the helium-vapor pumping on the quench threshold. The last section described the systematic-uncertainties study and the final recommendations for the beam intensity.

2 Magnetic Field Determination inside the Superconducting Magnet

The Magnetic field in the target region between the coils is 5 T with the homogeneity on the order of 10^{-4}. This level of homogeneity is critical for polarization of the target material as poor homogeneity limits the polarization achievable with DNP. The optimized region has a homogeneity of 8 cm along the z-direction and of 2.8 cm along the y-direction. The homogeneity along the up and down direction or the x-direction is approximately 5 cm. There is no information about the magnetic field in the coils or former or vacuum space around the coil dewar. It is also possible to measure the fridge field on the outside of the vacuum space but there is no trivial way to interpolate the magnetic field into the inaccessible regions inside the vacuum and coils volumes.

Figure 6 shows a sample of the measured magnetic field outside the magnet dewar which has a maximum field of 100 mT. The measurements were done during the November-2018 cooldown at UVA using Lakeshore Gauss meter. The uncertainty of the measurements is 20 mT. Over 300 measurement points were obtained, covering 5 horizontal planes and 4 azimuthal angles, as well as the radial and the vertical components of the field. The measurements matched with the simulation within the 20 mT uncertainty.

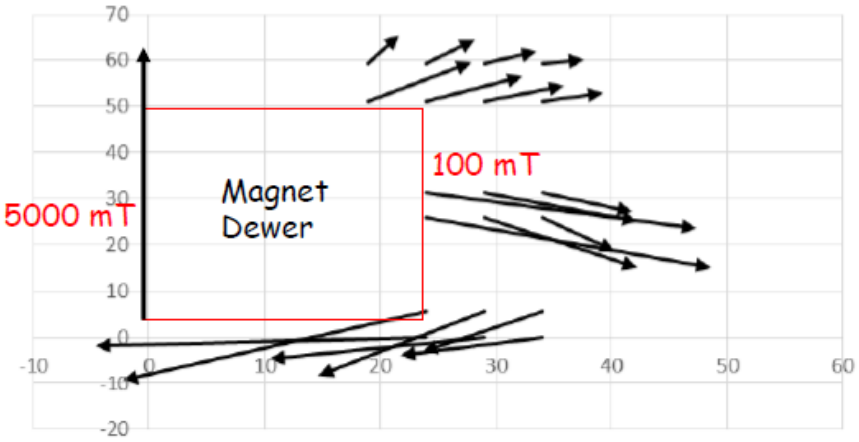

Figure 6: Sample of the magnetic field measurement outside the magnet dewar.

To perform this interpolation the superconducting coils were built in the COMSOL Multiphysics simulation framework with parameters tuned to match the measured magnetic field inside the target area and outside the dewar magnet, see figure 7.

The layout and geometry of the magnet dewar including the superconducting magnet is shown in figure 8. The design of the SpinQuest target magnet consists of a pair of three magnet coils forming a modified Maxwell coil providing a large

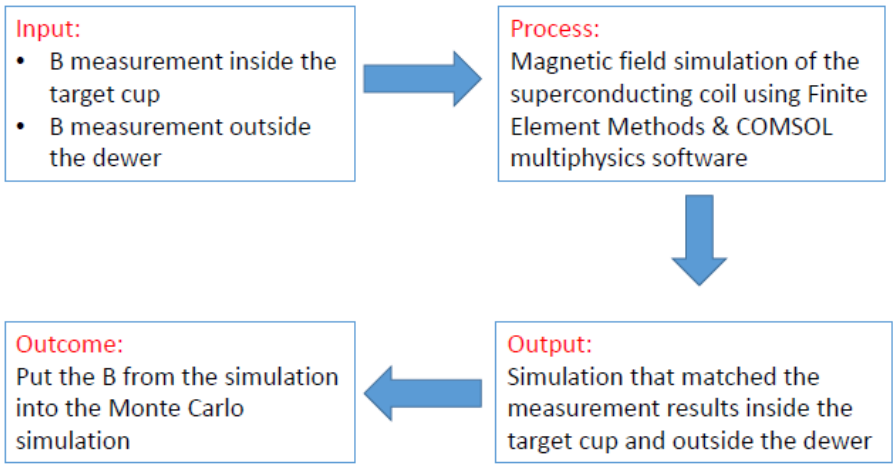

Figure 7: Simulation step to obtain the three-dimensional map of the magnetic field.

region of highly uniform magnetic field. A Maxwell coil is an improvement of the standard Helmholtz coil, with improved field uniformity over a larger region at the expense the additional coil and ultimately less opening. The length of the homogeneity in the x-direction is $\pm$ 2 cm. For high-energy experiments with beam energy greater than 100 GeV the scattering off the target is largely in the forward direction. The permits the use of a smaller opening for the beam exit.However, low energy secondaries can still spiral back into the coils to produce an additional heat load. The detected particle of SpinQuest are muons and are not largely effected by passing through the magnet materials either.

Assuming static current and field, the magnetic vector potential $\mathbf{A}$ must satisfy the following equation:

$$\nabla \times (\mu^{-1} \nabla \times \mathbf{A}) = \mathbf{J}, \tag{1}$$

where μ is the permeability, and $\mathbf{J}$ denotes the applied current density. The relations between the magnetic field $\mathbf{H}$, the magnetic flux density $\mathbf{B}$, and the potential are given by

$$\mathbf{B} = \nabla \times \mathbf{A} \tag{2}$$

and

$$\mathbf{H} = \mu^{-1} \mathbf{B}. \tag{3}$$

We set the relative permeability equal to 1 (vacuum) and treat the current density and the number of turns of the superconducting wire as free parameter. We adjusted these parameter to reproduce the measured magnetic field in the target area and outside the dewar. We have measured the vertical and radial components of the field outside the dewar. Over 300 points of measurement were

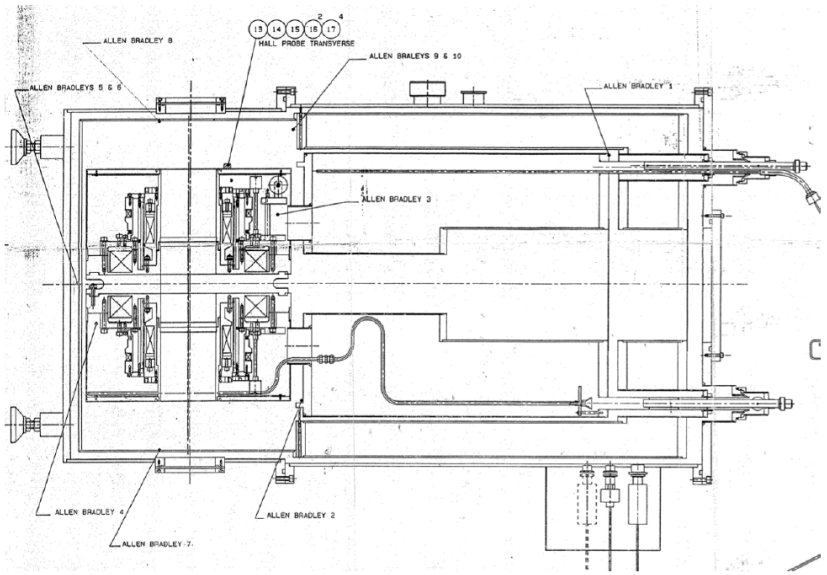

Figure 8: The layout of the magnet dewar including the superconducting-magnet.

performed using hall probe from Lakeshore Gausmeter, covering 5 horizontal planes, 4 azimuthal angles and up to 60 inches from the dewar's surface.

The set of partial differential equation are solved using Finite Element Method (FEM), implemented in COMSOL Multiphsics software. The FEM subdivides a large system into smaller, simpler parts called finite elements by the construction of a mesh of the object. The equations that model these finite elements are then assembled into a larger system of equations that models the entire problem. Figure 9 shows the mesh construction of the magnet model where tetahedral is used as the basic shape of the finite elements.

It is necessary to produce a 5 T field over the volume of the target cell with a homogeneity of 10^{-4}. Figure 10 shows the homogeneity of the field in the target cell region obtained from the simulation. Table 2 further shows the agreement of the magnetic-field strength in the target area obtained from the measurements and the simulation. Thus, we have obtained a three-dimensional map of the magnetic field inside the magnet dewar and vacuum space with good agreement between measurements and simulations. In the target region the simulation agrees with the NMR measurement within 10^{-4} T as shown in table 2. Outside the magnet dewar the simulation agrees with the hall probe measurement within device's uncertainty (20 mT).

probably we should just list a single value and error for each field point

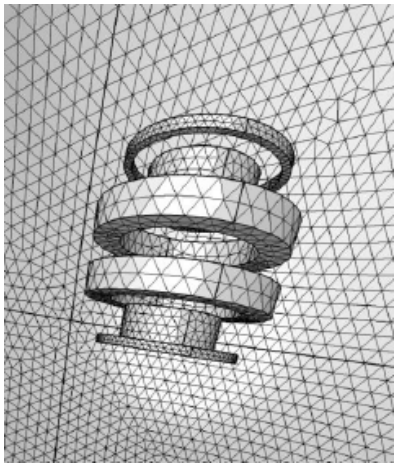

Figure 9: The construction of the tetahedral mesh for the magnet model.

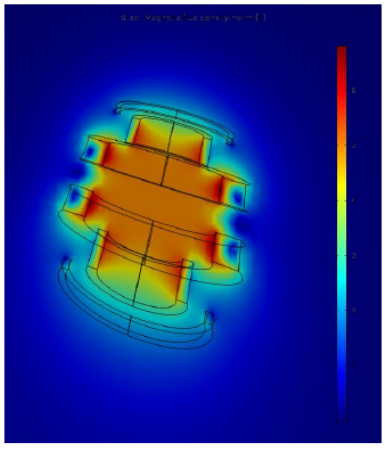

Figure 10: (Left) The magnetic field map in a cross-sectional plane of the magnet show the homogeneity of the field around the target area. (Right) The value of the magnetic field along the beam line in the target area.

Table 1: The value of the magnetic field in the target area obtained from the measurements and simulated field

z (cm)	y (cm)	Measurement (T)	Simulation (T)
-3.75 - 3.75	0.0	5.0195 - 5.0199	5.0192 - 5.0197
0.0	-2.0 - 2.0	5.0196 - 5.0197	5.0195 - 5.0197
3.75	-2.0 - 2.0	5.0190 - 5.0197	5.0191 - 5.0204

3 Thermal Analysis and Simulation of the Superconducting Magnet

The thermal process within the superconducting magnet is described by a general heat transfer equation

$$c\frac{\partial T}{\partial t} = \nabla(\kappa\nabla T) + P_{ext} + P_{He}, \tag{4}$$

where c is the volumetric heat capacity, T temperature, t time, κ thermal conductivity. P_{ext} is the heat flux from external heat sources per unit volume and P_{He} is the cooling heat flow to the liquid helium.

3.1 External Heat Sources (P_{ext})

The external heat sources in the superconducting magnet mainly come from the beam-target interaction. The collimator focuses the 120 GeV proton beam with the distribution profile shown in figure 11. The collimator limits direct beam-magnet interaction, but the secondary particles produced from the beam-collimator as well as beam-target interactions (figure 12) during the 4.4 s of the beam spill deposited a non-negligible heat that can lead to magnet quenching.

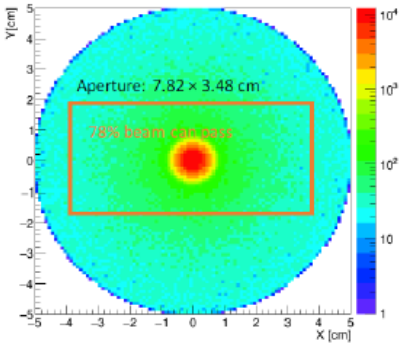

Figure 11: The Gaussian with exponential tail distribution of the proton-beam profile. The collimator allows 78% of the beam to passed to the target.

The amount of the heat deposited to the superconducting magnet from the beam-target and beam-collimator interactions were obtained form the Geant4 simulation. Figure 13 shows the average heat load for some slices of the superconducting magnet.

3.2 Cooling Processes by The Liquid Helium (P_{He})

The magnet coils are surrounded by a pool boiling 4.2 Kelvin reservoir. Helium has two liquid phases separated by a lambda line, $T_\lambda = 2.16$ K (see figure 14).

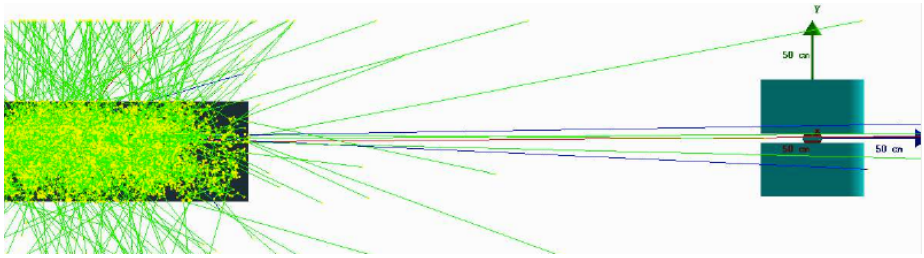

Figure 12: The illustration of the beam-target and the beam-collimator interactions. The beam tail is filtered by the 121.92 cm of collimator, showing on the left of the figure obtained from Geant4. The collimator allow the beam within the aperture to pass to the target. The target is polarized in the y-direction and sit within the magnet coils as shown on the right of the figure. The beam-aperture dimension is 7.82 × 3.48 cm

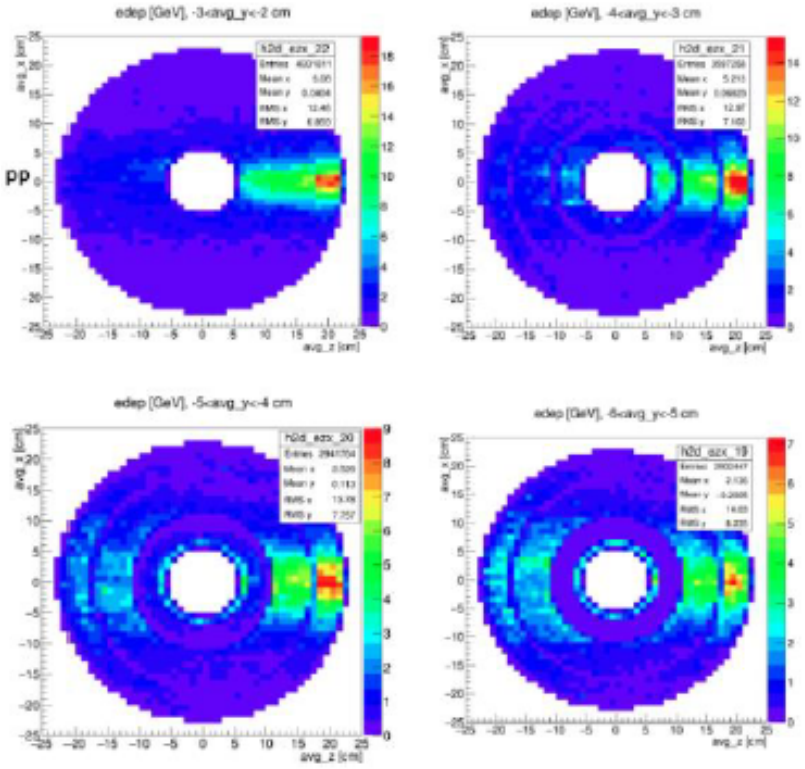

Figure 13: The heat deposited inside the magnet coils obtained from Geant4.

Left to the lambda line the helium is in the superfluid (He-II) phase, which has zero flow resistance (viscosity), and right of the line it is in a normal fluid (He-I) phase.

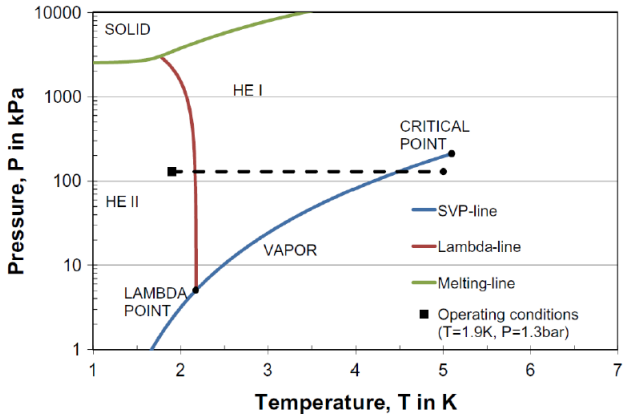

Figure 14: The He-phase diagram. The solid-red line is the lambda line, separating the superfluid phase (He-II) and the normal fluid phase (He-I) of the Helium. The solid-blue line show the SVP line that separate the vapor and liquid phase of the Helium. The solid-green line is the melting line which is the boundary of the solid and liquid phase of the Helium. The black-dashed line show the operating conditions of the SpinQuest experiment. NOTE: I will make my own figure.

The heat transfer between conductor and helium goes through several different regimes. The regimes which are relevant to the superfluid phase (He-II) are Kapitza regime and Film boiling regime. And the processes which are relevant in the normal-fluid phase (He-I) are natural convection, nucleate boiling, and film boiling regimes. We will only discuss the normal-fluid phase regime since the operating temperature are at above the lambda point.

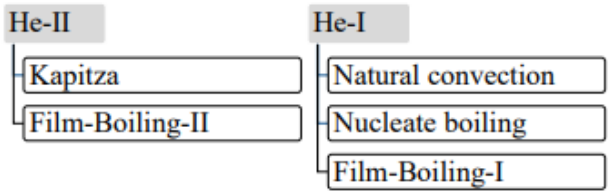

Figure 15: Different regimes of the heat transfer from solid to the liquid Helium.

Depending on the heating power, the heat transfer will start in the natural convection regime. It is followed by the nucleate boiling regime and finally it

enters the film boiling regime. Below a few W/(m^2) of heat flux to the liquid helium there is no phase change and cooling is assumed to be natural convection,

$$h(T_c, T_{He}) = a_{NC}(T_c - T_{He}), \tag{5}$$

where T_c is the temperature of the conductor surface, T_{He} is the temperature of the Helium, and the typical value of a_{NC} is 500 W/(m^{2}K). As the heat flux crosses the limit of natural convection (W/(m^2)), helium vapor is formed on the surface of the conductor. Then bubbles are formed which the rate of growth increase as the heat flux increase. As the bubbles detach from the surface, the cold liquid rush down to cool the surface. The amount of the heat flow for this nucleate boiling process is

$$h(T_c, T_{He}) = a_{NB}(T_c - T_{He})^{2.5}, \tag{6}$$

where the typical value of a_{NB} is 50000 W/(m^{2}K$^{-2.5}$). At a higher rate of the heat flux, the bubbles become unstable and they form a layer of helium vapor, preventing the liquid helium from being a direct contact with the conductor. The heat flow for this film boiling process is given by

$$h(T_c, T_{He}) = a_{FB}(T_c - T_{He}), \tag{7}$$

where the typical value of a_{FB} is 250 W/(m^{2}K).

Figure 16 shows The heat transfer regimes into the Helium bath from a heater for heat flows from 0.5 to 250 kW/m^2. The steady state of film-boiling regime is reached after approximately 0.1 second. Since The proton beam for the SpinQuest experiment run continuously for 4.4 second per spill, the steady state of film-boiling process (equation 7) is applied in this analysis.

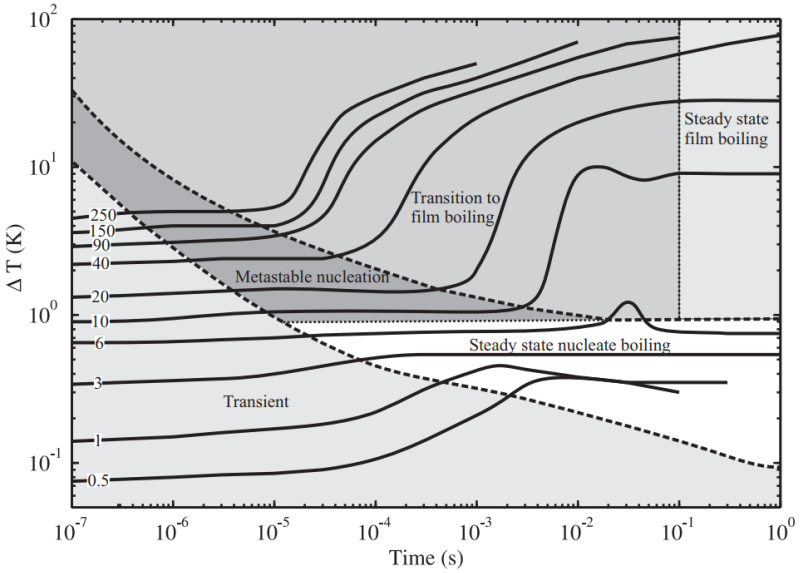

Figure 16: The heat transferred to the Helium in different regimes as a function of time. After approximately 0.1 second, the heat-transfer process reach steady state in the film-boiling regime.

3.3 Thermal Properties of the Materials

The basic element of the coils is the superconducting wire or strand where tiny (7 m) Nb-Ti filaments are bundled together in a number of hexagons and embedded in a copper matrix. Therefore, we need the thermal properties of the Nb-Ti in the superconducting state and the copper matrix to calculate the thermal properties of the composite materials that consist of of Nb-Ti superconductor and copper.

The superconducting coils are surrounded by 316LN stainless steel and impregnated in epoxy (see figure 17) to prevent them from moving due to the enormous amount of Lorentz force when the magnet is energized. Therefore, the materials that need to be considered are

- Nb-Ti superconductor
- Copper matrix
- The composite material consist of Nb-Ti superconductor and copper matrix
- 316LN stainless steel
- Epoxy

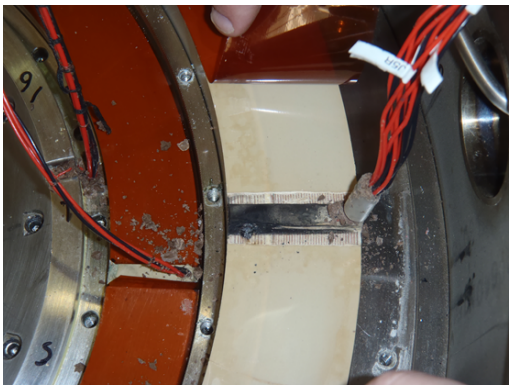

Figure 17: The superconducting wires impregnated in epoxy and further protected by 316LN stainless steel.

3.3.1 Thermal Conductivity

Thermal conductivity (κ) is defined as the ratio of the heat flux density to the temperature gradient. The physical unit for κ is WmK^{-1}. The thermal conductivity (κ) of the Nb-Ti superconductor can be approximated by

$$\kappa(T) = \sum_{0}^{6} a_n T^n, \tag{8}$$

where the parameters n are fitted from the measurements. There are two references which describe different value of n, summarized in table 3.3.1 below

Table 2: The fit parameters a_n of the Nb-Ti thermal conductivity from two references

a_n	Reference 1	Reference 2
a_0	6.6 $\times 10^{-2}$	6.81 $\times 10^{-2}$
a_1	4.56 $\times 10^{-2}$	-4.48 $\times 10^{-2}$
a_2	3.0 $\times 10^{-4}$	1.67 $\times 10^{-2}$
a_3	-3.0 $\times 10^{-6}$	-8.9 $\times 10^{-4}$
a_4	6.0 $\times 10^{-9}$	0
a_5	1.5 $\times 10^{-11}$	0
a_6	-5.0 $\times 10^{-14}$	0

Figure 18 shows the thermal conductivity of the Nb-Ti superconductor at $1 < \mathrm{T} < 10$ Kelvin from both references and the average value of them. We fitted the average thermal conductivity and the value can be approximated by

$$\kappa_{NbTi} = -0.0004\,T^3 + 0.0085\,T^2 + 0.0004\,T + 0.0671. \tag{9}$$

We use this average value for the simulation.

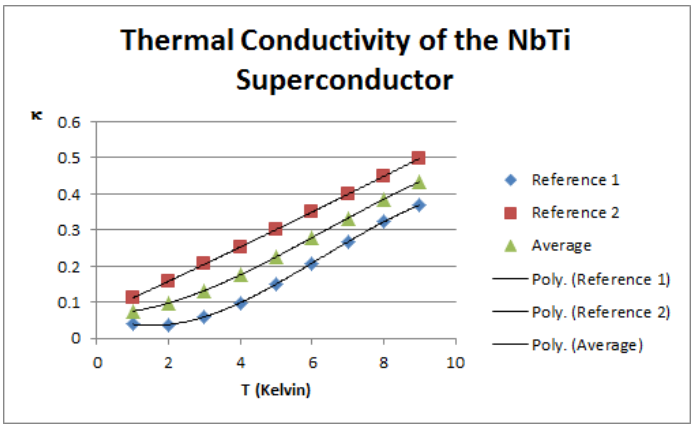

Figure 18: The thermal conductivity of the Nb-Ti superconductor from reference 1 (blue), reference 2 (red) and the average value of them (green).

According to the Wiedemann FranzLorenz (WFL) law, the thermal conductivity of copper or a pure metal in general can be calculated form the electrical resistivity by

$$\kappa = \frac{L_0 T}{\rho}, \tag{10}$$

where Ł$_0$ is the Lorenz number, $L_0 = 2.44 \times 10^{-8}$ (WΩK^{-2}) and ρ is the electrical resistivity. The electrical resistivity depends of copper depends on the applied magnetic field can be written as

$$\rho_{Cu}(B) = \frac{1.69 \times 10^{-8}}{RRR} + 5.02 \times 10^{-11} B. \tag{11}$$

RRR or residual resistivity ratio is a measure of the material's purity. RRR value is defined by the ratio of the electrical resistivity at two different temperature,

$$RRR = \frac{\rho(T = 273k)}{\rho(T = 4K)}. \tag{12}$$

The typical RRR values of the matrix copper in superconducting wires are between 100 to 200. In this analysis, we use $RRR = 150$. Combining equation 10 and 11, we could write the thermal conductivity of copper as

$$\kappa_{Cu} = \frac{L_0 T}{\frac{1.69 \times 10^{-8}}{RRR} + 5.02 \times 10^{-11} B}. \tag{13}$$

Figure 19 shows the thermal conductivity of the copper and the Nb-Ti superconductor in the log scale. The thermal conductivity of of Nb-Ti is 4 orders of magnitude smaller than that of Cu.

We use the Rayleigh model to determine the thermal conductivity of the composite. The model based on a continuous matrix reinforced with parallel cylindrical fillers arranged in uniaxial simple cubic array (see figure 20).

Thermal conductivity of the composite is directional dependent. If z is the axis of the filler (Nb-Ti), the effective thermal conductivity in the longitudinal direction is

$$\kappa_{eff}, z = \kappa_{Cu} + (\kappa_{NbTi} - \kappa_{Cu})\, \phi, \tag{14}$$

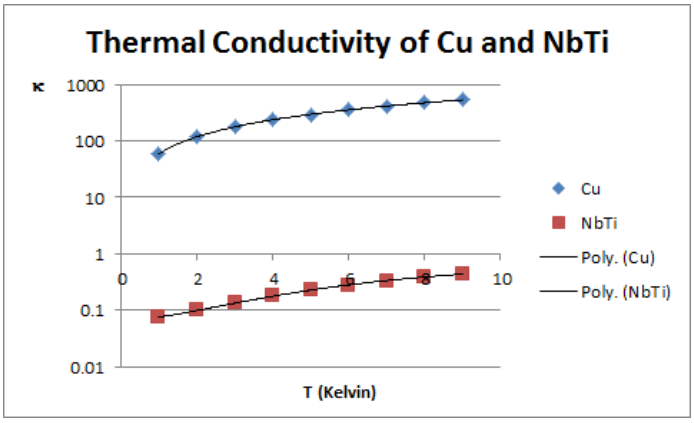

Figure 19: The thermal conductivity of the copper and the Nb-Ti superconductor.

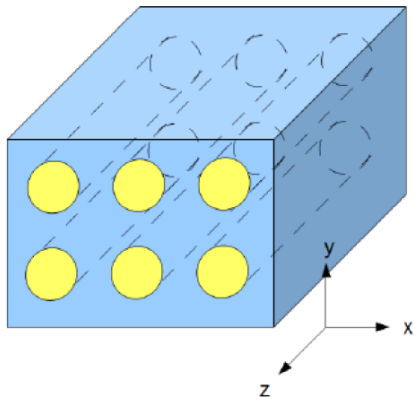

Figure 20: The schematic of the composite medium considered by Rayleigh, consisting of parallel cylinders embedded in a continuous matrix.

and the effective thermal conductivity in the transverse direction is

$$\kappa_{eff}, T = \kappa_{Cu} + \frac{2\kappa_{Cu}\phi}{C_1 - \phi + C_2(0.30584\phi^4 + 0.013363\phi^8 + ...)}, \tag{15}$$

where ϕ is the volume fraction of the Nb-Ti (we use $\phi = 0.4$), and

$$C_1 = \frac{\kappa_{NbTi} + \kappa_{Cu}}{\kappa_{NbTi} - \kappa_{Cu}}, \tag{16}$$

$$C_2 = \frac{\kappa_{NbTi} - \kappa_{Cu}}{\kappa_{NbTi} + \kappa_{Cu}}. \tag{17}$$

Figure 21 shows the thermal conductivity of the composites in both directions along with the thermal conductivity of the constituents (Copper and Nb-Ti). In this analysis, we use the average value of κ_{eff}, z and κ_{eff}, T and applied this value for all directions of thermal propagation in the composites. These average values (shown in figure 22) are polynomial fiited and can be approximated by

$$\kappa_{eff}(T) = -0.0003T^3 + 0.0051T^2 + 40.414T - 0.0402. \tag{18}$$

The thermal conductivity of the 316 stainless steel could also be approximated by

$$\kappa_{316LN}(T) = \sum_{0}^{6} b_n T^n, \tag{19}$$

where the parameters n are fitted from the measurements and summarized in table 3.3.1. This equation is valid at $2 < T < 50$ Kelvin. Figure 23 shows the thermal conductivity of 316LN stainless steel at $2 < T < 9$ Kelvin.

Epoxy resin is used in the manufacturing of superconducting magnet in particular for the thermal and electrical insulation due to its low thermal conductivity. Figure 24 shows the thermal conductivity of three epoxy measured

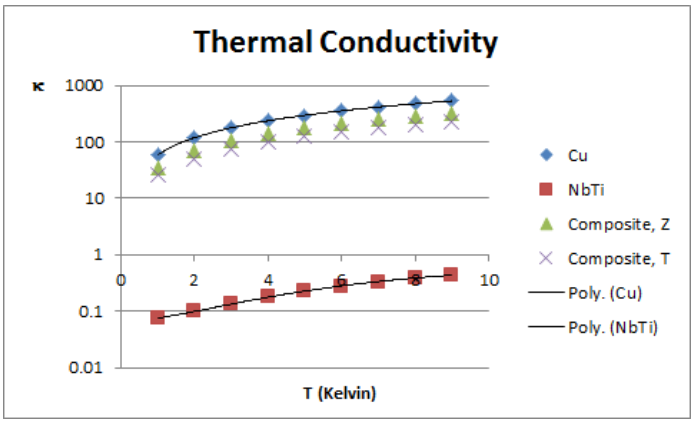

Figure 21: The thermal conductivity of the composite in the longitudinal and transverse directions.

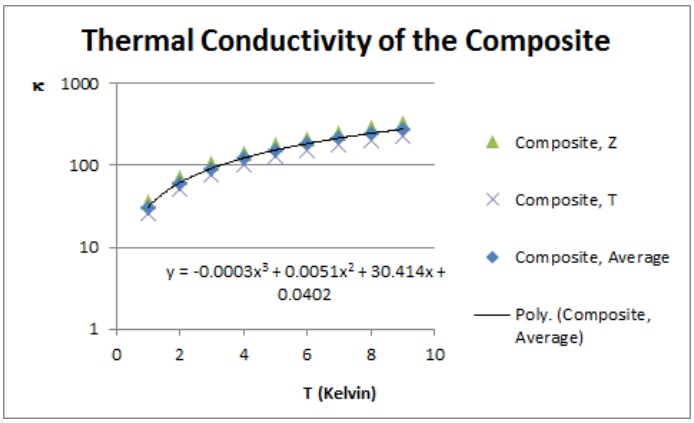

Figure 22: The average thermal conductivity of the composite (solid line fit), applied to all directions of the thermal propagation.

in []. The thermal conductivity is relative constant at below 10 Kelvin, range from 0.05 to 0.1 $\mathrm{Wm^{-}1K^{-}1}$. We use $\kappa_{epoxy} = 0.075\ \mathrm{Wm^{-}1K^{-}1}$ in our analysis.

3.3.2 Density

The density of materials can be changed by changing the temperature, following

$$\frac{\Delta\rho}{\rho(T = 300K)} = 1 - \left(1 + \frac{\Delta L}{L}\right)^3, \tag{20}$$

where $\Delta L/L$ is the thermal contraction factor. Table 3.3.2 shows the thermal contraction factor for some metals. Since the thermal contraction factor for

Table 3: The fit parameters b_n of the 316LN stainless steel thermal conductivity.

b_n	Value
b_0	-7.75 $\times 10^{-2}$
b_1	6.93 $\times 10^{-2}$
b_2	1.35 $\times 10^{-3}$
b_3	5.92 $\times 10^{-5}$
b_4	-4.11 $\times 10^{-6}$
b_5	9.28 $\times 10^{-8}$
b_6	-7.59 $\times 10^{-10}$

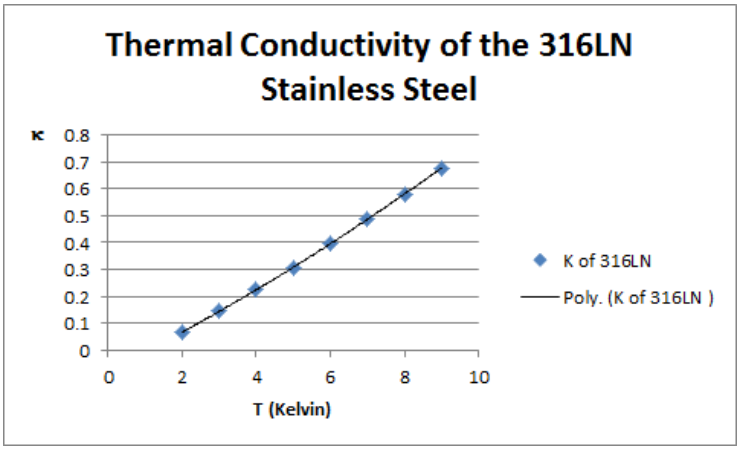

Figure 23: The thermal conductivity of the 316LN stainless steel.

solids in general are small, we can treat the density value as constant.

Element/Material	Symbol	20 K	80 K	200 K
Copper	Cu	.00323	.00302	.00149
Brass	65Cu-35Sn	.00380	.00350	.00169
Aluminum	Al	.00412	.00390	.00201
Lead	Pb	.00700	.00577	.00263
Invar	Fe-Ni36	.00046	.00048	.00020
Araldite		.01050	.00880	.00500
Titanium	Ti	.00151	.00142	.00073
Austenitic steel	316LN	.00297	.00278	.00138

Table 4: The thermal contraction parameters for some metals.

The density for the superconducting wire as a composite material consist of

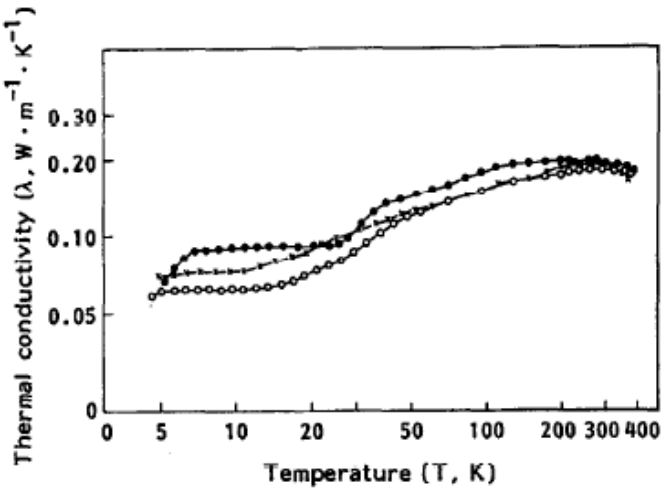

Figure 24: The thermal conductivity of the epoxy resin from three different samples [].

Nb-Ti and copper matrix is

$$\rho_{sc} = \phi\,\rho_{NbTi} + (1 - \phi)\,\rho_{Cu}, \tag{21}$$

where ϕ is the volume fraction of the Nb-Ti (40%). The density all materials involved in this analysis are summarized in the table 3.3.2 below.

Table 5: The density of the solid materials involved in the analysis

material	density (Kg/m^{-3})
Nb-Ti	6000
Copper	8960
Superconducting wire	7776
316LN Stainless steel	7990
Epoxy	1200

3.3.3 Heat Capacity

Specific heat is the amount of energy needed to raise the temperature of a material by 1 K. We will use the spesific heat under constant pressure with the unit of JKg^{-1}K^{-1}. The specific heat of the Nb-Ti superconductor depends on the magnetic field and under 9 Kelvin can be approximated as

$$C_{NbTi} = 0.0082T^3 + 0.011BT. \tag{22}$$

The specific heat of copper at low temperatures could also be approximates using polynomial fit as

$$C_{Cu} = -3.44\times10^{-6}\,T^4 + 8.1\times10^{-4}\,T^3 - 2.38\times10^{-4}\,T^2 + 1.14\times10^{-2}\,T - 2.86\times10^{-4}. \tag{23}$$

The specific heat of the superconducting wire could also be obtained from the specific heat of Nb-Ti and copper,

$$C_{sc} = \phi\,C_{NbTi} + (1-\phi)\,C_{Cu}, \tag{24}$$

where ϕ is the volume fraction of the Nb-Ti (40%). Figure 25 shows the specific heat of the Nb-Ti, copper and the superconducting wire. The specific heat of the wire could be approximated as

$$C_{sc} = 0.0037\,T^3 + 0.0001\,T^2 + 0.0325\,T + 0.0003. \tag{25}$$

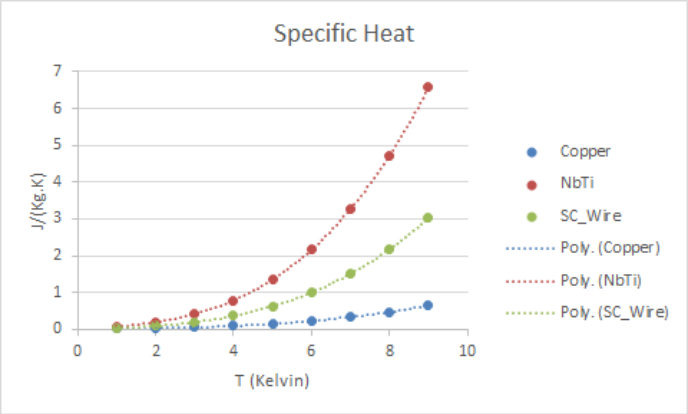

Figure 25: The specific heat of the Nb-Ti, copper and the superconducting wire.

The specific heat of the 316LN Stainless steel is fitted to

$$C_{316LN} = 0.48\,T + 0.00075\,T^3. \tag{26}$$

The specific heat of epoxy-resin measured experimentally and shown in figure 26, plotted as CT^{-3} versus temperature. According to this figure the specific heat at $2 < T < 9$ K in J/m^{3}K could be approximated as

$$C_{epoxy} = 50T^3, \tag{27}$$

and we need to divide by the density of epoxy to transform the unit into J/(KgK). Figure 27 shows the specific heat of epoxy along with the specific heat of the superconducting wire and 316LN Stainless steel.

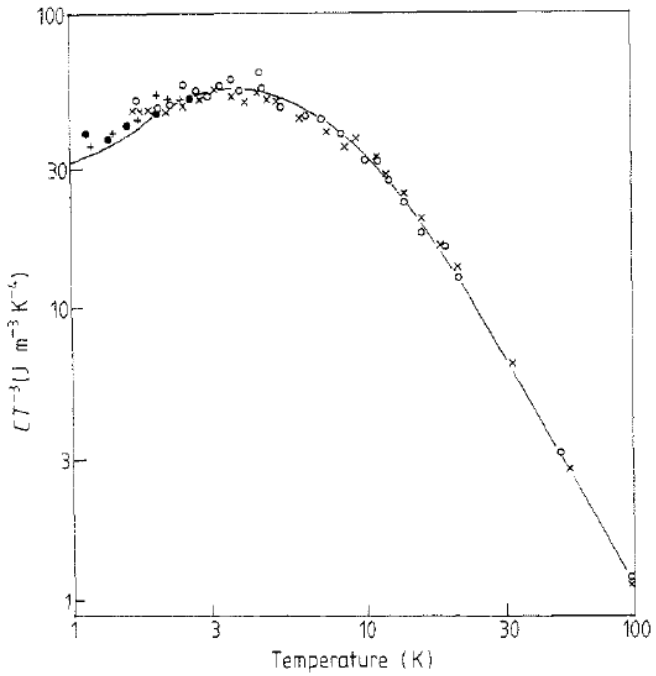

Figure 26: The specific heat of two samples of epoxy-resin, plotted as CT^{-3} versus temperature.

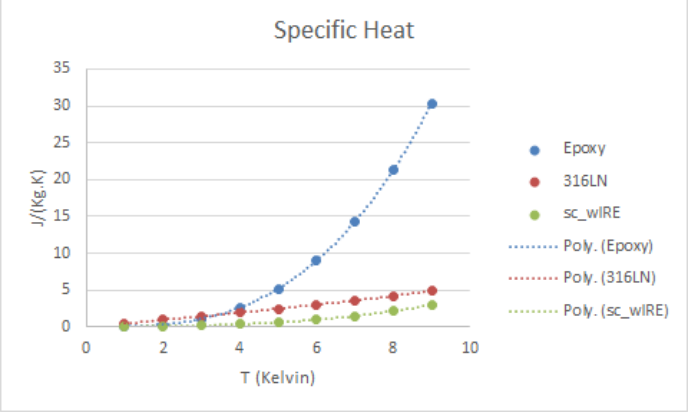

Figure 27: The specific heat of the epoxy-resin, 316LN Stainless steel and the superconducting wire.

4 Simulation

The proton beam will be delivered in a spill which is 4.4 second long every minute. The time structure of the beam is illustrated in figure 28 below.

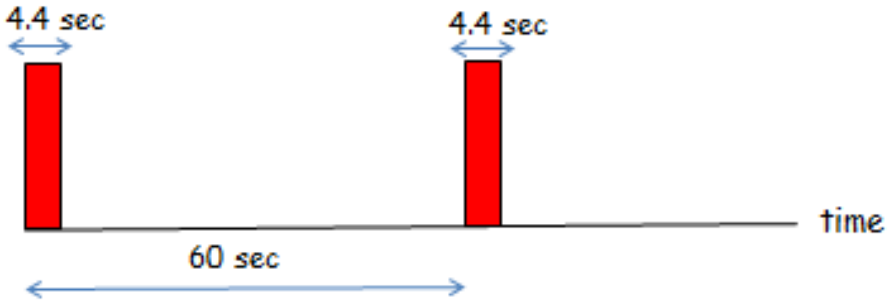

Figure 28: The time structure of the proton beam showing 4.4 second long per spill.

The temporal profile of the beam is one of the important input for the simulation along with the thermal properties of the materials and the heat transfer processes.

The simulation were performed using COMSOL Multiphysics, a commercial software dedicated to perform Finite Element Analysis for solving non-linear differential equations. COMSOL provides the temperature profile in the discretized geometry as a function of time. We studied several geometrical models of the superconducting magnet and compare the simulation results.

4.1 3-Dimensional model

In 3-Dimensional model (3D) we considered the superconducting magnet as of a uniformly mixture of the superconducting wire and epoxy and then treat them as one material with effective thermal properties. The superconducting magnet is surrounded by 316LN stainless steel. The top surface of the magnet and the stainless steel are in a direct contact with the liquid helium. Therefore, the convection is only happen at the top surface of the magnet and the stainless steel former.

Figure 29 shows the temperature distribution at the end of the first beam spill, $t = 4.4$ s in the magnet and the former. The hot spot in the magnet are spread uniformly due to the high thermal conductivity of the chopper matrix. The hot spots are still exist in the stainless steel due to its lower thermal conductivity. Figure 30 show the maximum temperature in the magnet as a function of time. The maximum temperature increase up to 6.1 K for each beam spill and then down to the base temperature (4.2 K) before the next spill. Both figures use 1×10^{12} proton/sec as the beam intensity.

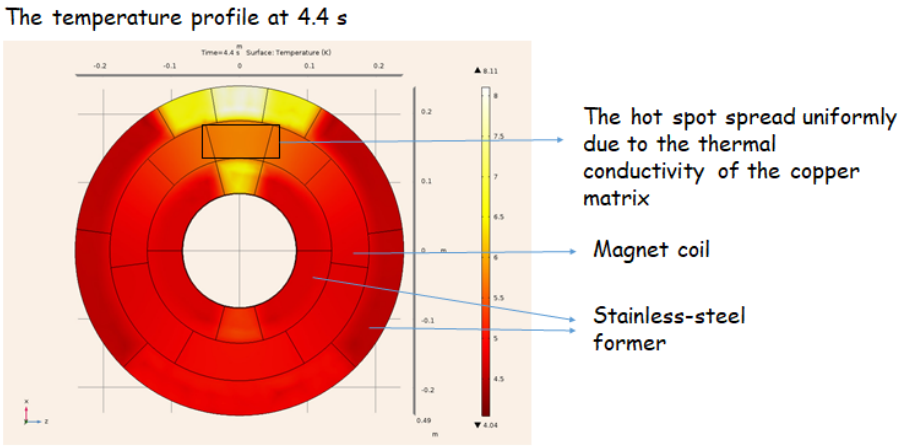

Figure 29: The temperature distribution in the superconducting magnet and the stainless steel former at the end of the beam spill ($t = 4.4$ s).

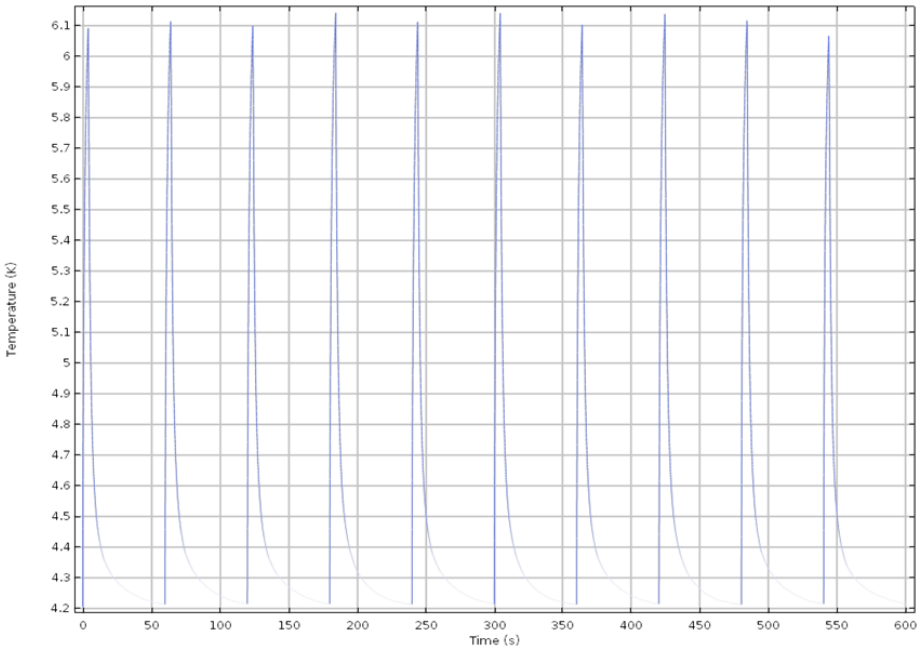

Figure 30: The maximum temperature in the magnet as a function of time. The temperature peak is 6.1 K for each spill and down to the liquid helium temperature before the next beam spill.

5 Quench Threshold

The critical temperature of the superconducting wire as a function of magnetic field $T_c(B)$ is

$$T_c(B) = T_{c0}\Big(1 - \frac{B}{B_{c20}}\Big)^{0.59}, \tag{28}$$

where T_{c0} and B_{c20} for the Nb-Ti superconducting wire is $T_{c0} = 9.2$ K and $B_{c20} = 14.5$ T. The magnetic field in the magnet is obtained from the simulation, shown in figure 31. The maximum field is 6.85 T and according to the equation 28 the critical temperature of the magnet is 6.3 K. The maximum temperature with the beam intensity 1×10^{12} proton/sec is 6.1 K as shown in figure 30. Therefore, we consider 1×10^{12} proton/sec as the maximum beam intensity for the NH3 target that the superconductor magnet could handle before quench.

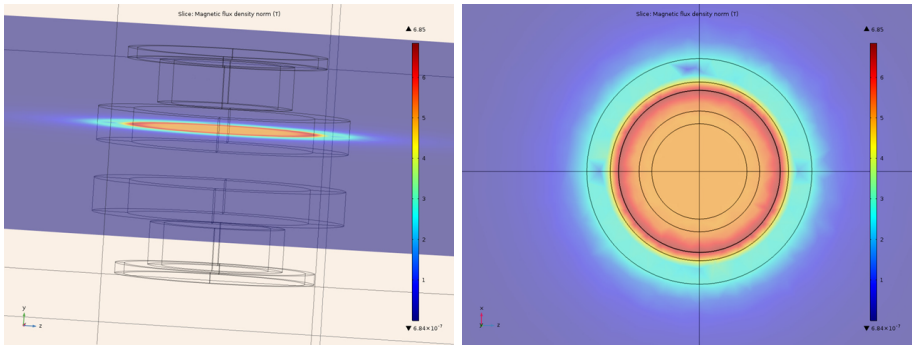

Figure 31: The magnetic field distribution inside the superconducting magnet. The maximum field is 6.85 T.

6 Beam Stability Issue

During the E906 experiment (SeaQuest) the beam intensity was not constant. The bucket-by-bucket intensity varies greatly and sometimes the beam intensity jump in the order of nano second (ns). The SeaQuest experiment applied the programmed inhibit threshold that is set to veto RF buckets above the desired intensity, which shown as red line in figure 32. Therefore, we need to understand whether the superconducting magnet survive when the beam intensity jump in the order of ns.

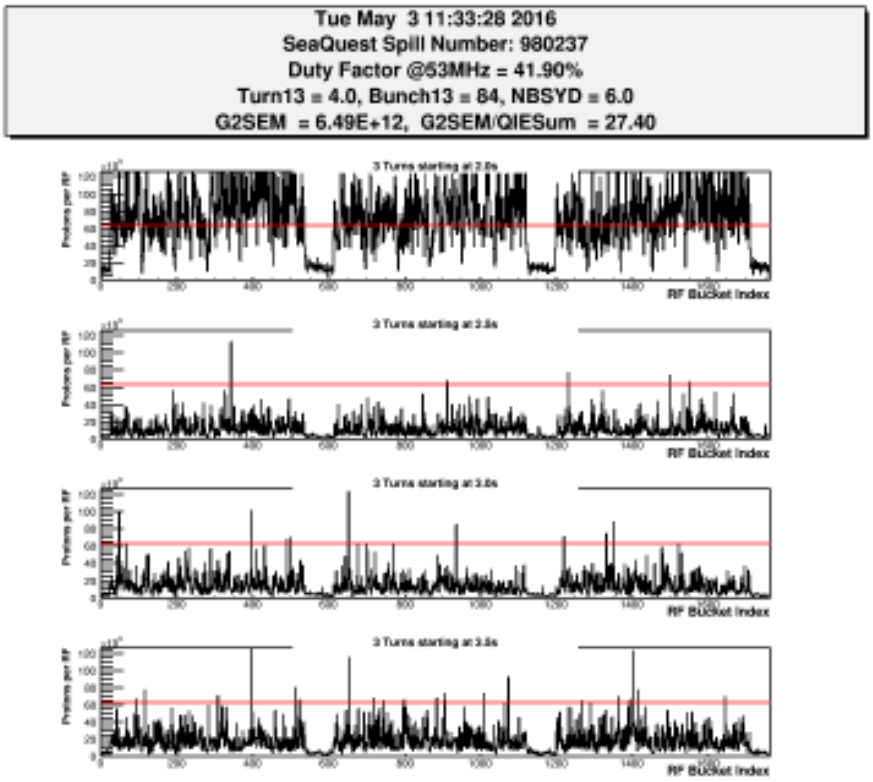

Figure 32: The proton intensity per RF bucket delivered to SeaQuest experiment. The red line shows the programmed inhibit threshold that is set to veto RF buckets above the desired intensity.

Unfortunately, COMSOL could not handle the time step in the order of ns. We then solved the problem analytically with some approximations applied. We assumed the heat deposited in the magnet do not diffused during the beam jump (ns). Therfore, we could set the thermal conductivity, $\kappa = 0$. Thus, we could

write equation 4 as

$$c\frac{\partial T}{\partial t} = P_{ext} + P_{He}. \tag{29}$$

If the assumption is correct, we should see better agreement between analytical solutions and simulations as the jump time going smaller. We calculated and simulated the maximum temperature in the magnet if the beam jumped up to ten times of the desired intensity during the duration of $\Delta t = 0.2, 0.15, 0.125$ and 0.1 second.

The maximum temperature on the magnet derived from the equation 29 is

$$T_{max}(K) = \sqrt{42.868 \times I \times t + 17.64}, \tag{30}$$

where I is the scale factor of the jump intensity and t is the jump duration. Table 6 shows the comparison between the calculation and simulation. As we expected, the difference between analytical solutions and simulations (ΔT) is going smaller as the duration of the beam jump decrease. Hence, we can rely on the analytical solution for the maximum temperature in the magnet during the nano second period of the beam jump, which shows, according to equation 30 that the temperature increases is negligible. In conclusion, we do not need to worry about the beam intensity jump as long as the duration is in the order of ns.

Table 6: The maximum temperature in the magnet during the beam jump obtained from the analytical solution and simulation.

"Jump" intensity	Duration of the jump	Tmax Comsol (K)	Tmax Calculation (K)	Delta T
10 times	0.2	7.3	10.2	2.87
10 times	0.15	7	9.05	2.05
10 times	0.125	6.7	8.44	1.74
10 times	0.1	6.3	7.78	1.48

7 The Effect of Helium Vapor Pumping on the Magnet Reservoir

7.1 Pumping the Helium Vapor on the Magnet Reservoir using KNF Pump

The simulations (and calculations) that we did so far are based on the liquid helium temperature of $T = 4.2$ K. We can reduce the liquid helium temperature by pumping the helium vapor from the magnet reservoir. Figure 33 shows the relation between the vapor pressure and the liquid helium temperature for ^{3}He and ^{4}He. In principle, we could low the temperature of the ^{4}He down to $\sim$0.5 K if we have zero heat leak by pumping the reservoir continuously. Unfortunately, zero heat leak is extremely difficult to achieve but the base temperature of $T \approx 2.5$ K is reasonable instead. We will use KNF pump with the speed of maximum 100 Standard Liter per Minute (SLPM) to pump the Helium vapor. Assuming the base temperature of $T = 2.5$ K, we have the following questions:

- What is the new intensity of the proton beam that could quench the superconducting magnet?
- What is the helium vapor rate produced in the magnet reservoir?
- Is the vapor rate exceed the KNF pumping capacity?

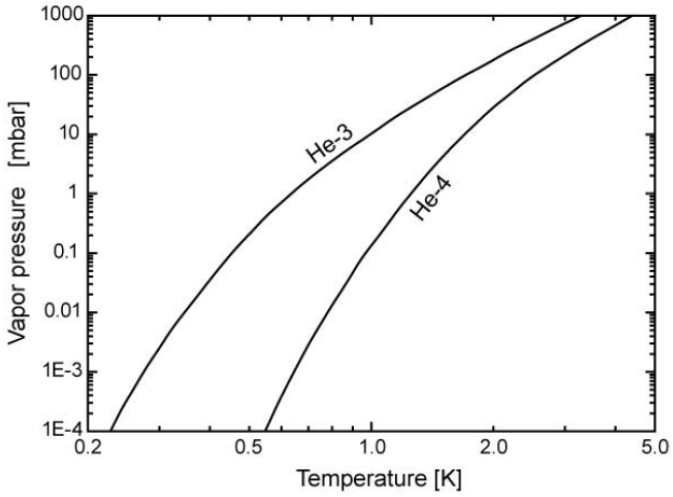

Figure 33: The vapor pressure versus temperature of the ^{4}He and ^{3}He.

Figure 34 shows the maximum temperature in the magnet with the intensity of 1×10^{12} proton/sec. Pumping the vapor out of the magnet reservoir bring the

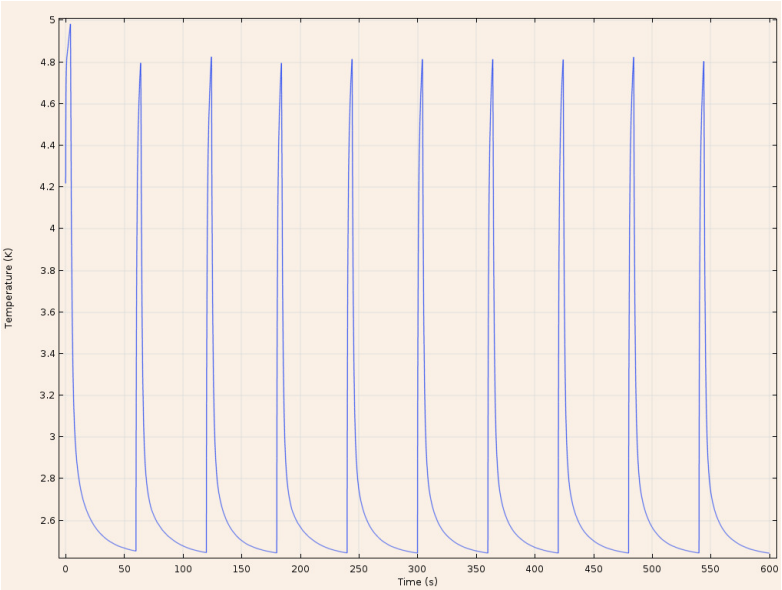

Figure 34: The new maximum temperature in the magnet when we pumping the helium vapor out of the magnet reservoir. The peak temperature in now 4.8 K.

maximum temperature down to 4.8 K. Therefore, we could potentially increase the beam intensity.

Figure 35 shows the maximum temperature in the magnet with the pump on and the beam intensity is 3.2×10^{12}. The maximum temperature peak is 6.1 K which is right in the quench threshold. Therefore, we can conclude that pumping out the helium vapor give us a room to increase the beam intensity up to 3.2×10^{12} maximum.

Figure 36 shows the temperature on the top surface of the magnet and the former. The peak temperature is 6 K. We can use this information to calculate the production rate of the helium vapor. The total heat released to the helium during the beam spill is

$$Q_{He} = hA(T - T_{He})t, \tag{31}$$

Where h is the convective heat-transfer coefficient, $h = 250$ W/(m^{2}K), A is the surface area, $A = 0.12$ m^2, T is the peak of the surface temperature, $T = 3.6$ K,T_{He} is the liquid helium temperature, $T_{He} = 2.5$ K, and t is the beam-spill duration, $t = 4.4$ s.

The volume of the He-vapor produced in 1 minute is

$$V = 22.4 \times \frac{Q_{He}}{L_{He}}, \tag{32}$$

where L_{He} is the latent heat of the helium. Putting all the numbers together

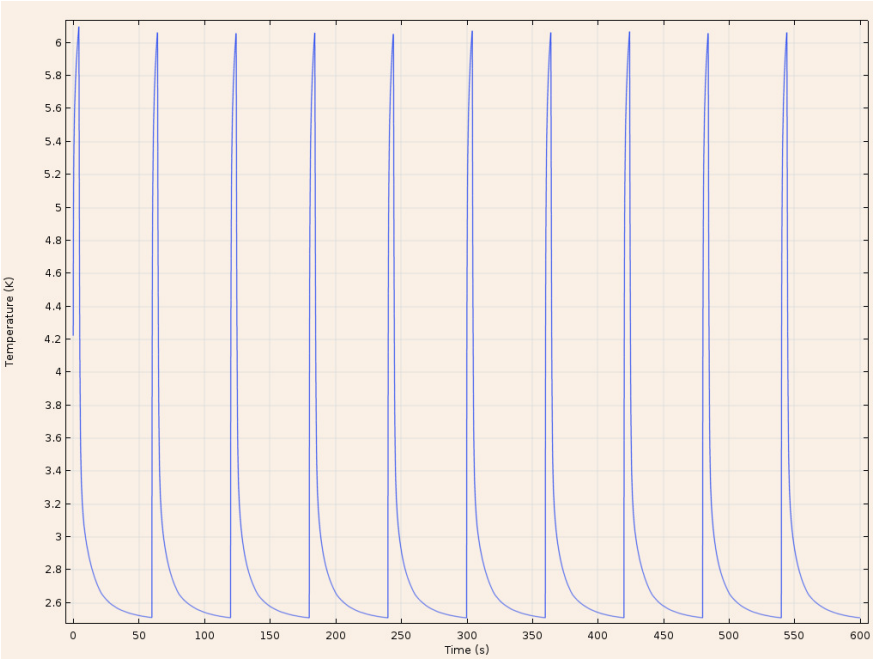

Figure 35: The maximum temperature in the magnet with the increase of beam intensity up to 3.2×10^{12} proton/sec.

we get $V = 38.3$ liter/min which is still below the maximum pumping capacity.

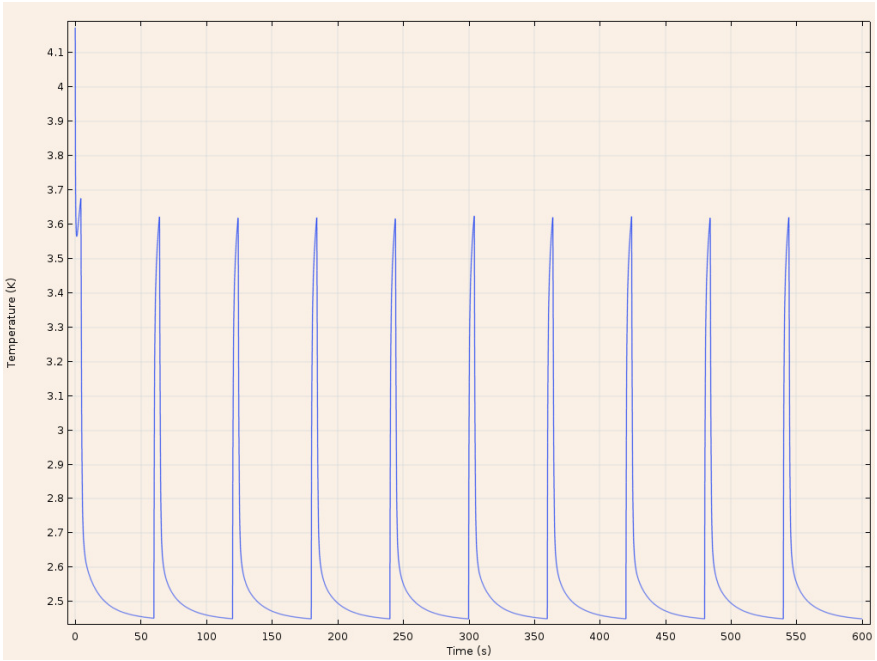

Figure 36: The top-surface temperature in the magnet with the increase of beam intensity up to 3.2×10^{12} proton/sec.

7.2 Pumping the Helium Vapor on the Magnet Reservoir using Sogevac Pump

The Sogevac SV630 is the backing pump for the Root pumps, which are the main pumps to maintain the target temperature at around 1 K. The Sogevac SV360 could maintain He-vapor pressure of 2 mbar or liquid-Helium temperature at T_{He} =1.3 K according to the Helium pressure vs temperature diagram shown in figure 33. By default, the liquid-Helium reservoir is connected to the KNF pump, but pumping the He vapor using Sogevac pump instead only requires a small modification, which is installing a short and flexible pipe from KNF line to Sogevac SV630. The Sogevac and KNF pumps are placed next to each other on cryo platform as shown in figure 37 below.

Once the Roots pumps are in full operation, the Sogevac pump only does a little work. Thus, using the Sogevac pump with the capacity of 700 m^3 per hour open more possibility to lower the liquid-Helium temperature and increase the beam intensity.

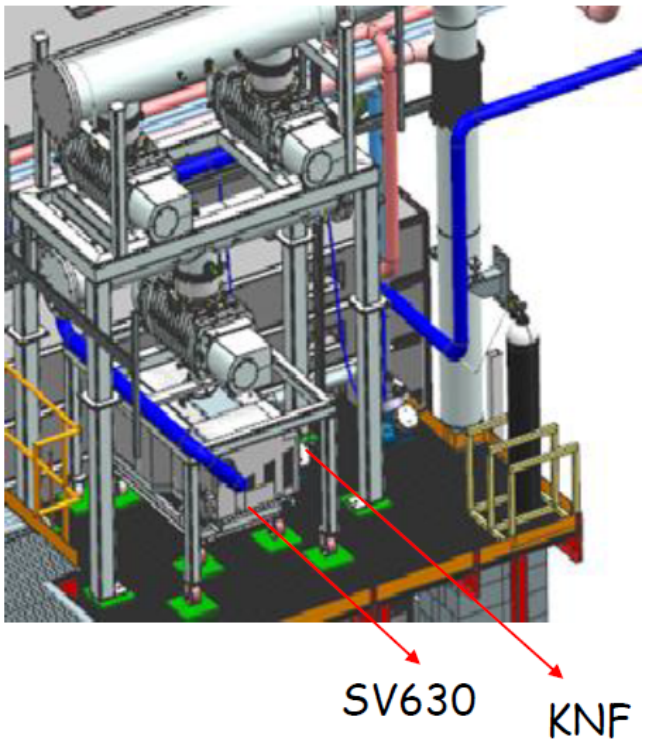

Figure 37: The Sogevac SV360 and KNF pumps on cryo platform.

Figure 38 shows the maximum temperature on the superconducting magnet if we pump the Helium vapor using Sogevac SV630 pump for the beam intensity of 4.2 $\times 10^{12}$ proton/sec. The maximum temperature almost reach the quench

threshold (T =6.3 K) for this intensity. Therefore, pumping the Helium vapor from the magnet reservoir using Sogevac SV630 pump open the possibility to increase the beam capacity to 4.2×10^{12} proton/sec.

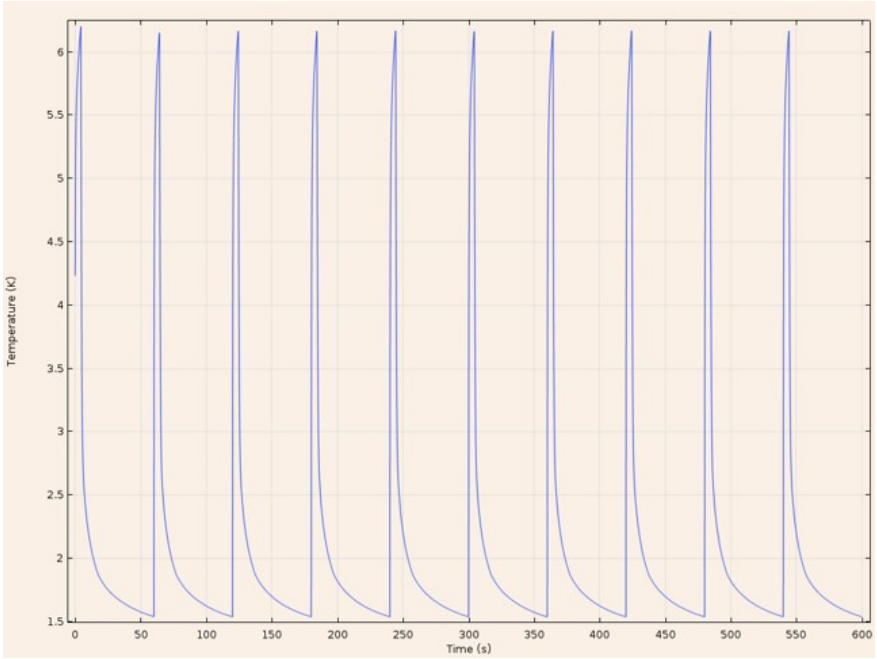

Figure 38: The maximum temperature in the magnet with the increase of beam intensity up to 4.2×10^{12} proton/sec.

8 Thermocouple Sensors Installation on the Magnet Reservoir

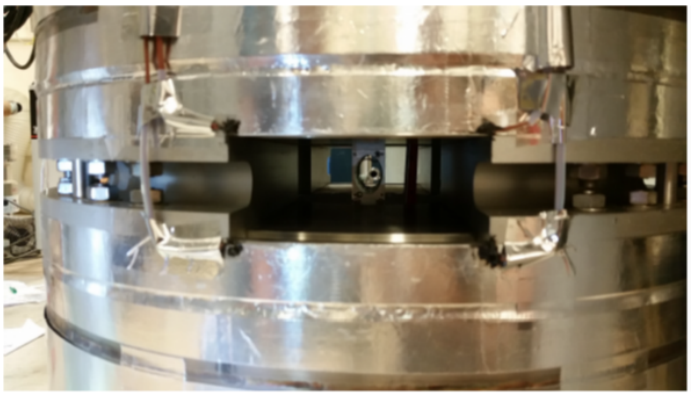

Figure 39: The type-T thermocouple sensors installed on the surface of the magnet reservoir.

Unfortunately, we do not have the access to measure the temperature of the superconducting magnet directly during the experiment. What we can measure is the temperature on the magnet-reservoir surface (stainless steel former). 8 type-T thermocouple sensors are installed on the reservoir surface as shown in figure 39. 4 sensors are installed upstream and 4 sensors are installed downstream with respect to the beam direction. Those sensors function to test the temperature predictions from COMSOL simulations. Therefore, we also need to generate temperature predictions on the sensors. Figure 40 shows the temperature predictions for the upstream (green line) and downstream (blue line) sensors as a function of time. The maximum temperature on the upstream sensors is 6.5 K and the maximum temperature on the downstream sensors is 5 K. Both figures use 1×10^{12} proton/sec as the beam intensity.

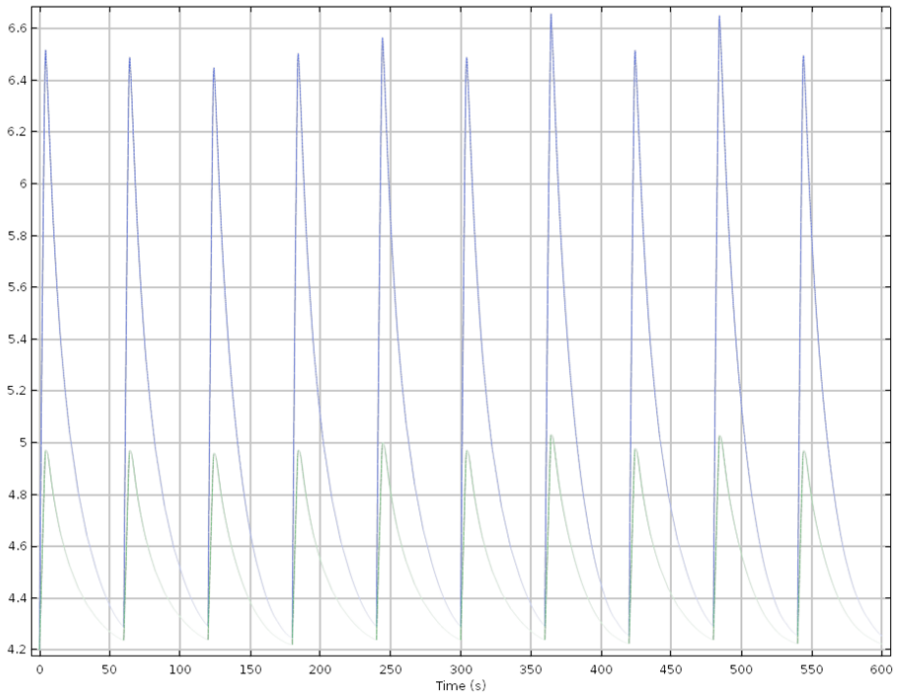

Figure 40: The temperature predictions of the upstream (green line) and downstream sensors (blue line) as a function of time. The peak temperature of the upstream sensors is 5 K and the peak temperature of the downstream stream is 6.5 K.

9 Systematic study

The systematic uncertainties for the maximum temperature in the magnet were obtained by varying critical parameters that affect the heat deposited in the magnet. The first parameter that we studied is the choice of the Geant-physics list. Figure 41 shows the difference in the heat deposited to the superconducting magnet from two different Geant-physics options: FTFP-BERT and QGSP-BERT.

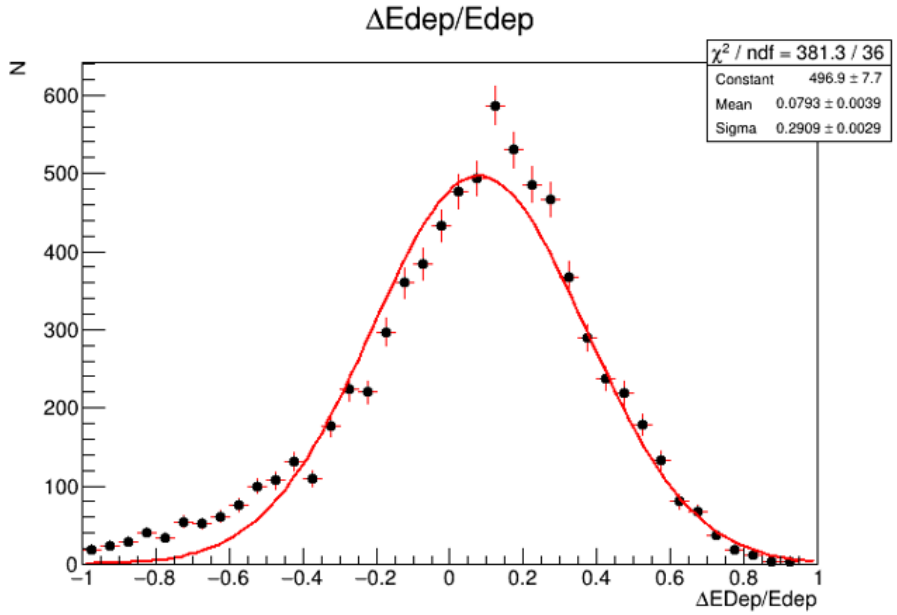

Figure 41: The differences of the heat deposited in the superconducting magnet based on the FTFP-BERT and QGSP-BERT physics options.

The difference of the heat deposited in the magnets as shown in figure 41 is defined as

$$\frac{\Delta Edep}{Edep} = \frac{E_{FTFP-BERT} - E_{QGSP-BERT}}{E_{FTFP-BERT}}. \tag{33}$$

The gaussian fit to the distribution resulted in the mean of 0.079. We took 7.9 % as the systematic uncertainty of the heat load due to the choice of the geant-physics list. Then we investigated how the uncertainty on the heat load affect the uncertainty in the maximum temperature if the magnet by varying the heat load according to the uncertainty (7.9 %). We found that the maximum temperature in the magnet differ by 2.21 % (no pumping) and 2.81 % (KNF pumping) as we varied the heat load by 7.9 %.

We also studied the uncertainties due to the possibility of the beam drift. If the beam position drift from the center of the target, the heat load could have

non-negligible differences. Figure 42 shows the differences of the heat deposited in the magnets when the beam drift by 3 mm from the center of the target. The mean of the gaussian fit to this distribution is 0.061. We took 6.1 % as the systematic uncertainty on the heat load due to the beam drift. Following the same procedure, we varied the heat load by 6.1 % and found the maximum temperature in the magnet differ by 1.72 % for no pumping and 2.2 % for KNF pumping.

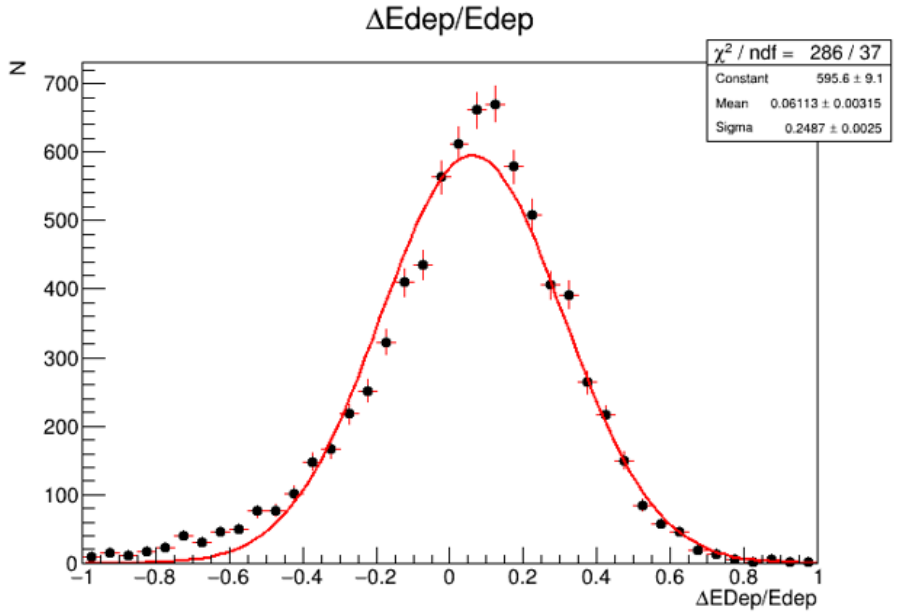

Figure 42: The differences of the heat deposited in the superconducting magnet if the beam drift by 3 mm from the target center.

The Geant-physics options and the beam drift are two among many aspects of the systematic uncertainties on the maximum temperature that we studied. We have also studied how the uncertainties on the maximum temperature depend on the uncertainty of the material properties, the heat transferred to the LHe and the COMSOL simulations. The full list of those aspects are shown in table 7,8 and 9.

The total systematic uncertainties of the maximum temperature for both pumping scenario are shown at the end of table 9. For no-pumping scenario, Beam intensity of 1×10^{12} proton/sec resulted in maximum temperature of 6.1 K with uncertainty 4.5 % (6.1 K $\pm$ 0.27 K). The KNF-pumping scenario with the beam intensity of 3.2×10^{12} proton/sec resulted in maximum temperature of 6.1 K with uncertainty 5.8 % (6.1 K $\pm$ 0.35 K).

Table 7: The systematic uncertainties on the heat load and the corresponding uncertainties on the maximum temperature for no pumping and KNF pumping.

Subsystem	Systematics	ΔTmax/Tmax (No pump)	ΔTmax/Tmax (KNF Pump)
External Heat Sources			
Geant Pysics List	7.8 %	2.21 %	2.81 %
Beam drift	6.1 %	1.72 %	2.2 %
SC wire Density			
• Density uncertainty	7 %	0.61 %	0.94 %
• Thermal contraction factor	0.3 %	0.03 %	0.03 %
• Volume fraction	8 %	0.27 %	0.42 %
SC wire Specific heat			
• Measurement uncertainty	20%	1.7 %	2.5 %
• Volume fraction	8%	0.89 %	1.13 %
• Magnetic field	3.4 %	0.02 %	0.06 %

Table 8: The systematic uncertainties on the heat load and the corresponding uncertainties on the maximum temperature for no pumping and KNF pumping.

Subsystem	Systematics	ΔTmax/Tmax (No pump)	ΔTmax/Tmax (KNF Pump)
SC wire Thermal Conductivity			
• NbTi Measurement uncertainty	45%	0.02 %	0.03 %
• Volume fraction	8%	0.18 %	0.23 %
• Magnetic field	3.4%	0.24 %	0.27 %
• Copper RRR	50%	0.08 %	0.12 %
• Rayleigh model uncertainty	25%	0.3 %	0.41 %
316LN Density			
• Density uncertainty	1.13 %	0.08 %	0.097 %
• Thermal contraction factor	0.3 %	0.02%	0.03 %
316LN Specific heat			
• Measurement uncertainty	2%	0.13 %	0.17 %
316LN Thermal Conductivity			
• Measurement uncertainty	2%	0.24 %	0.29 %

Table 9: The systematic uncertainties on the heat load and the corresponding uncertainties on the maximum temperature for no pumping and KNF pumping.

Subsystem	Systematics	ΔTmax/Tmax (No pump)	ΔTmax/Tmax (KNF Pump)
Heat transferred to the LHe			
• Coefficient uncertainty	50 %	0.7 %	1.1 %
• Contact-surface area	50 %	0.7 %	1.1 %
COMSOL Simulation			
• Mesh	Normal, fine, extra fine	0.79 %	0.8 %
• Time Step	Δt = 0.05 .. 0.001	Negligible	Negligible
• Geant fitting	10%	2.6 %	3.1 %
TOTAL		**4.5 %**	**5.8 %**
		6.1 K +/- 0.27 K	**6.1 K +/- 0.35 K**

10 Summary and Recommendation

The SpinQuest experiment at Fermilab will utilize a target system consisting of a 5T superconducting magnet. In order to protect the magnet during the experiment, a quench needs to be avoided. For this, a proper understanding of how the magnet temperature increase due to the external heat source is essential. Thus, A quench analysis and simulation in the superconducting magnet using COMSOL were performed to determine the maximum intensity of the proton beam before the magnet quench. Based on the magnetic-field mapping, the quench threshold for the magnet is 6.3 K. Considering the uncertainties described in the previous section, the maximum intensity of the beam proposed for SpinQuest experiment is shown in table 10 below.

The heat deposited in the coils are mainly from the beam-target interaction. The target ladder, NMR coils and target cups contribute $\sim$ 15 % of the total heat load in the magnet. There is still a lot of room to increase the beam intensity by reducing the heat deposited in the magnet coils from scattering off of insert materials. Configuring the best position for the target ladder depends on our alignment accuracy and machining tolerance of the insert,. Putting the NMR coils outside the cells also can reduce the background scattering. Its also possible to make an insert with a low-profile ladder with little material interacting with the beam.

In summary, applying KNF-N0150 pumping to the magnet dewar make it possible to increase the beam intensity up to 2.7×10^{12} proton/s. Without pumping, the maximum intensity before quenching the magnet is 8.5×10^{11} considering the uncertainty on the simulation.

Table 10: The final recommendations of the beam intensity.

PUMP	BEFORE SYSTEMATIC STUDIES (PROTON/SEC)	AFTER SYSTEMATIC STUDIES (PROTON/SEC)
No pumping	1×10^{12}	0.85×10^{12}
KNF-N0150	3.2×10^{12}	2.7×10^{12}

Pumping the Helium vapor using the Sogevac SV630 instead the KNF pump open the possibility to increase the beam intensity further. Considering the systematic study, the upper limit of the beam intensity with the Sogevac-SV630 pumping is 3.5×10^{12} proton/s.

References

[1] R. L. Jaffe and A. Manohar, Nucl. Phys. B **337**, 509 (1990).

[2] C. A. Aidala, S. D. Bass, D. Hasch and G. K. Mallot, Rev. Mod. Phys. **85**, 655 (2013).

[3] A. Deshpande, Prog. Theor. Exp. Phys. **2015**, 03A107.

[4] K. F. Liu *et al.*, PoS LATTICE **2011**, 164 (2011).

[5] D. Sivers, Phys. Rev. **D41**, (1990) 83.

[6] A. Airapetian *et al.* [HERMES Collaboration], Phys. Rev. Lett. **103**, 152002 (2009).

[7] M. Alekseev *et al.* [COMPASS Collaboration], Phys. Lett. **B673**, 127 (2009).

[8] X. Qian *et al.* [JLab Hall A Collaboration], Phys. Rev. Lett. **107**, 072003 (2011).

[9] A. Klein, D. Keller, spokesperson, "SeaQuest with a Transversely Polarized Target (E1039)", Proposal to Department of Energy.

[10] C. Keith, Private communication.

[11] P. Bauer. "Stability of Superconducting Strands for Accelerator Magnet," Doctoral Dissertation (1998), TU Wien.

[12] G. Willering. "Stability of Superconducting Rutherford Cables," Doctoral Dissertation (2009), University of Twente.

[13] D. Paudel. "Quench Simulation of Superconducting Magnets with Commercial Multi-Physics Software," Master Thesis (2015), Aalto University.

[14] J. Y. Jang, Y. J. Hwang, M. C. Ahn and Y. S. Choi, Physica C: Superconductivity and its application **550**, (2019) 99-106.

[15] K. Pietrak, and T. S. Wisniewski, Journal of Power Technologies **95 (1)**, (2015) 14-24.

[16] E. Haro. "Simulation Tool Development for Quench Modelling," Doctoral Dissertation (2016), Tampere University of Technology.

[17] L. E. Evseeva and S. A. Tanaeva, Cryogenics **35**, (1995) 277-279.

[18] S. Kelham and H. M. Rosenberg, J. Phys. C: Solid State Phys **14**, 1737 (1981).

[19] S. Russenschuck (2011). "Field Computation for Accelerator Magnets," John Wiley & Sons, Ltd.

[20] L. Rossi and M. Sorbi, "MATPRO: A Computer Library of Material Property at Cryogenic Temperature," CARE-Note-2005-018-HHH (2006).

[21] P. Bauer, H. Rajainmaki and E. Salpietro, "EFDA Material Data Compilation for Superconductor Simulation," EFDA Memo (2007).

[22] K. Hock, "Cooling Techniques," Lecture notes of PHYS393, University of Liverpool (2011).